Image-based finite element modelling of fibre dynamics in polyester staple spun yarns

Haoqi Zhang [a,b], Abdul Jabbar [c,d], Aonan Li [b], Xinxin Wang [e], Dongmin Yang [b,*], Muhammad Tausif [c]

[a] School of Advanced Manufacturing, Sun Yat-Sen University, Shenzhen, 518107, Guangdong, China
[b] School of Engineering, Institute for Materials and Processes, University of Edinburgh, EH9 3FB, United Kingdom
[c] School of Design, University of Leeds, Leeds, LS2 9JT, United Kingdom
[d] Department of Textile Engineering, National Textile University, Faisalabad, 37610, Pakistan
[e] School of Traffic & Transportation Engineering, Central South University, Changsha, 410075, Hunan, China

ARTICLE INFO

ABSTRACT

This paper introduces an innovative finite element (FE) modelling approach for fibre dynamics in a staple spun yarn based on the geometrical model derived from X-ray microcomputed tomography (μCT) images. The FE model retains crucial in situ information on fibre anisotropy, length, and continuity while employing advanced stitched scanning technique to reconstruct a 15 mm yarn length containing individual fibres with ~10 μm diameter. The research focuses on 100 % polyethylene terephthalate (PET) staple ring-spun yarn as a case study, conducting both single fibre and yarn tensile tests to characterise material properties and validate the FE model, respectively. Beyond examining the mechanical response at the yarn level, the model facilitates the investigation of individual fibre's tensile stress, frictional forces, and extent of migration, thereby enhancing the understanding of fibre interactions during yarn tensile loading. Furthermore, the model enables parametric studies through manipulation of inter-fibre friction coefficients allowing assessment of their impact on overall mechanical behaviour. This innovative modelling approach demonstrates significant potential for exploring the constitutive and failure mechanisms for formation of microplastics from textiles and textile materials in general as well as fibre-reinforced composites. It addresses the critical research gaps in simulating anisotropic behaviours of materials containing textile fibres, paving the way for advanced material design and analysis.

1. Introduction

Fibrous materials, as well as their derivative fabrics and fibre-reinforced composites, play significant roles in driving innovation across various engineering and scientific disciplines. Their versatility and unique properties have led to extensive adoption across a broad spectrum of industries including aerospace, automotive, construction, medical, and consumer goods, among others, where they contribute significantly to advancements in technology and product development [1–3]. The release of fibrous microplastics, also known as fragmented fibres, from all textiles poses a significant global environmental concern. Throughout their lifecycle, textiles shed fibre fragments (fibrous microplastics), contributing to the growing issue of microplastic pollution [4]. The underlying mechanisms leading to generation and release of fragmented fibres are yet fully elucidated. The intrinsic material

properties of constituent fibres, as well as the structural architecture of fibrous materials, play a crucial role in influencing fibre dynamics under various stress conditions during textile manufacturing, use, and service.

Fibrous materials are distinguished by their slender and elongated morphology typically characterised by diminutive diameters at micro-scale. Their formation processes involving stretching or spinning, impart a pronounced anisotropy along the fibre direction [5,6]. Consequently, fibrous materials typically exhibit higher strength and stiffness when subjected to tensile forces, while displaying increased pliability and susceptibility to deformation in the transverse direction. The fracture of fibre fragments from constituent fibres and their release to environment causes fragmented fibre pollution. Moreover, their anisotropic properties extend beyond mechanical performance, influencing other functionalities such as optical transmission, thermal conductivity, and electrical conductivity [7–10]. Understanding these intricacies in

material behaviour underscores the crucial importance of considering material orientation and structural geometry, beyond fragmented fibres pollution, in design and engineering applications enabling the optimal exploitation of their unique properties and potential.

To comprehend the performance intricacies of fibrous materials and refine their structural design, numerical simulations have become increasingly pivotal. These simulations delve into the intricate interactions between fibres and fibre/matrix, aiming to unravel the mechanisms governing fibre action and reinforcement at the microscale [11,12]. However, the accuracy of these simulations hinges largely on the geometric models utilised, encompassing aspects such as fibre positions, orientations, relative fractions, and continuity. In the past, in simplifying the derivation of geometric models, some researchers employed a simplification strategy, representing fibrous materials as ideal structures [13,14], abstracting away from their complex real-world characteristic. These structures portrayed each fibre in the yarn following a constant helical path around the yarn axis [15–17] or continuous straight fibres uniformly dispersed in fibre-reinforced composite materials [18,19]. Nonetheless, the actual geometric configurations of fibrous materials prove exceedingly intricate and irregular. They encompass features such as fibre disorder and breakage, often precipitating stress concentrations and subsequent failure [20].

To address these challenges, some researchers have endeavoured to develop more robust geometric models by incorporating statistical or distributional parameters to accommodate irregularities [21,22]. They developed random geometric models based on these statistics and material distributions, coupled with finite element analysis, to predict the mechanical behaviour of fibrous materials with more accuracy [23]. However, the process of establishing random geometric models through statistical distributions inevitably leads to some loss of geometric specificity, resulting in distortions during analysis. These distortions are further exacerbated when multiple irregularities are combined [24]. For instance, the complexity of staple spun yarn structure is influenced by multiple factors, including fibre migration, variable twist, variations in packing density across the cross-section, and discontinuous fibre lengths [25]. The cumulative effect of these irregularities diminishes the effectiveness of randomly generated models in simulating fibrous materials, highlighting the need for more sophisticated approaches.

To accurately capture the complex full real-life geometry of materials, it is imperative to utilise characterisation methods that probe their internal three-dimensional (3D) structures. Among these methods, X-ray micro-computed tomography (µCT) stands out as a powerful method, employing X-rays to generate precise cross-sectional images of physical objects, thereby enabling the creation of virtual 3D models without destroying the original sample [26]. This technology allows for imaging at pixel sizes as small as 100 nm, rendering it well-suited for detailed fibre tracking and structure analysis of fibrous materials [27]. Previous research has developed algorithms based on skeletonisation to track individual fibres in low-density fibrous materials [28,29] which were then extended for yarn analysis [30]. Furthermore, the high-fidelity geometric models extracted from µCT images were integrated with finite element analysis of yarn structure using beam elements, intending to investigate the behaviour under axial and transverse loads [25].

Despite advancements in fibre tracking algorithms and µCT-based modelling of fibres and yarns, as mentioned in the previous sections, a critical knowledge gap exists. To the authors' best knowledge, the generated yarn geometric models have not adequately addressed the key features of fibrous materials, namely the anisotropy and the interaction between fibres and fibre/matrix. Furthermore, a fundamental trade-off exists between achieving high-resolution cross-sectional images for precise fibre tracking (at the micrometre level) and capturing a representative length of slender yarn (at millimetre level). Consequently, only a model with a sufficient length and microscale fibre details can accurately simulate the fibre interaction within specific yarn structure, thereby bridging this knowledge gap.

To address the above research gap, this study aims to propose a novel

numerical method for developing high-fidelity and anisotropic finite element models based on in-situ µCT images of fibrous materials, thus enabling the image-based modelling. The method considers yarn structures longer than 10 mm and tracks individual fibres within the yarn body with diameters ~10 µm, facilitating the analysis of the micro-behaviour of individual fibres and their interactions. In this paper, 100 % PET ring-spun yarn is selected as the research subject as PET is the most commonly employed textile polymer and ring spun yarns are the most common yarn structure employed. Two µCT datasets, *i.e.*, a 0.8 mm segment and a 15 mm stitched dataset, are utilised to develop high-fidelity and anisotropic models, facilitating a comparative analysis. Through simulations of yarn stretching and experimental validation, the impact of parameters such as friction behaviour on the models is studied. The successful identification of individual fibres also enables the anisotropic models to conduct a detailed analysis of stress distribution at the microscale, fibre migration during dynamic processes, and inter-fibre frictional behaviour. This innovative numerical approach presents a valuable tool for the micro-analysis of yarn structure, with potential applicability to other fibrous materials and fibre-reinforced composites exhibiting anisotropy enabling a deeper understanding of their complex behaviours.

2. X-ray microcomputed tomography and reconstruction

This section provides an overview of the scanned ring-spun yarn samples and the µCT scanning setup. As previously mentioned, a stitched scanning technique was employed to accommodate yarn structure models with lengths surpassing a helical cycle. We detail the image processing involved in stitching an extensive µCT dataset exceeding 10 mm in length, along with the data processing methods for tracking fibre centrelines using Avizo software.

2.1. µCT scanning

100 % polyethylene terephthalate (PET) staple ring-spun yarn, from a commercially relevant short staple spinning system, was selected for µCT scanning and microstructural analysis. The yarn was produced with a nominal linear density of 29.53 tex (20.0's Ne). The twist level was kept at 7.04 turns.cm^{-1} (17.88 turns.inch^{-1}). The surface topography of ring-spun yarn is shown in Fig. 1c which shows that the ring yarn has a helical arrangement of fibres in the yarn body.

The Zeiss Xradia 620 Versa in the National X-Ray Computed Tomography Centre at the University of Manchester, UK, was employed to conduct µCT scanning. As shown in Fig. 1b, the yarn samples for µCT scanning were carefully prepared by mounting yarns in the centre of a Kapton® tube (5 mm internal diameter) along its length and applying an appropriate pre-tension to remove slackness and are held stationery during scanning. The scanning process was started by mounting the Kapton® tube in the µCT scanning stage vertically with respect to incident X-ray beam and aligning it along the field of view of µCT scanning system. Fig. 1a shows the scanning setup in Zeiss Xradia 620 Versa system. For a regular scanning, the yarn specimen was fully rotated by 360°, resulting in 3201 projections collected on a noise-suppressed 2000 × 2000 pixels charge-coupled detector. Further, the stitched scanning was performed, which involved 11 times regular scanning along the yarn length, with a slight overlap between adjacent segments. Table 1 presents the technical specifications for µCT scanning and details of scanning results are shown in Figs. 2 and 3. In comparison, the stitched scanning technique requires more scanning time in total and greater stability of Zeiss system, as well as additional data stitching of 11 scanned segments (with more than 1.5 mm length for each). As a result, it allows the acquisition of µCT datasets with the length exceeding 10 mm for the yarn and the resolution to 10 µm for each individual fibre, which also makes the scanning results more reliable and representative.
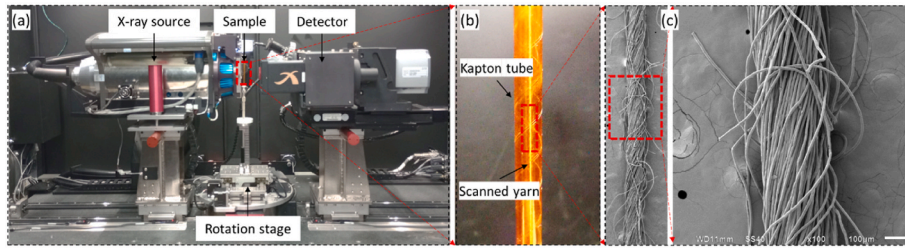
Fig. 1. (a) Scanning setup in Zeiss Xradia 620 Versa (b) Yarn specimen mounted in the Kapton® tube (c) Surface topography of 100 % PET staple ring-spun yarn used in the study.

Table 1
Detailed specifications of µCT scanning.

Parameters	Regular scanning	Stitched scanning
Resolution/voxel (µm)	0.81147	0.827
Number of segments/blocks	1	11
Total cross-sectional images along the length	960	19710
Total scanned length of yarn (mm)	0.7782 (1 × 0.7782)	15.574 (11 × 1.5 with overlap)
X-ray energy (KV) × (µA)	80 × 125	80 × 125
Exposure time (seconds)	3	3

2.2. Image processing and µCT data stitching

Due to significant displacement of the scanning field when transitioning between segments (as shown in Fig. 2a), automatic stitching of µCT datasets with more than 10 segments using the Zeiss system is not feasible. To address this issue, a Python algorithm was developed based on the analysis of central points of the yarn obtained from the cross-sectional images. The initial step in image processing involves noise removal using Median Filter followed by the application of Watershed Separation to generate the binary image for fibre areas, as shown in Fig. 2b & c.

The central point of the yarn body is determined using the 'Measure' function in ImageJ and marked in red. These central points of multiple cross-sectional images are then connected to form the yarn's centreline along the z-axis. For two adjacent segments, a slight overlap of 10 cross-

sectional images (approximately 8 µm in length along the z-axis) is initially introduced.

The algorithm calculates the differences in the x-y plane coordinates of the central points between upper and lower segments within this overlap area (resulting in 10 differences during the first calculation), and the standard deviation of these differences is recorded. The overlap area is then extended with additional cross-sectional images, and a new standard deviation is recorded. The corrected overlap area is identified when the standard deviation reaches a minimum (nearly zero), indicating that the centreline of upper segment in this overlap area aligns with the centreline of lower segment in the x-y plane. Since the yarn's centreline is a microscale curve, a coordinate standard deviation close to zero can only be obtained when the overlap area along z-axis is correctly identified, as shown in Fig. 2d. Consequently, the overlap dataset can be removed using the above algorithm, and the x-y plane coordinates between the two adjacent segments are corrected. This method of stitching the two adjacent segments allows for the merging of µCT datasets into a yarn exceeding 10 mm in length, facilitating the further tracking of each individual fibre.

2.3. Centreline tracking

To track the centreline of each individual fibre, the X-Fibre module in Avizo software is employed, which involves following four sub-steps:

i) A visual cylinder template is created by selecting a fibre segment in a slice and adjusting its length and radius to fit the cross-section, as illustrated in Fig. 3a. The template's length and
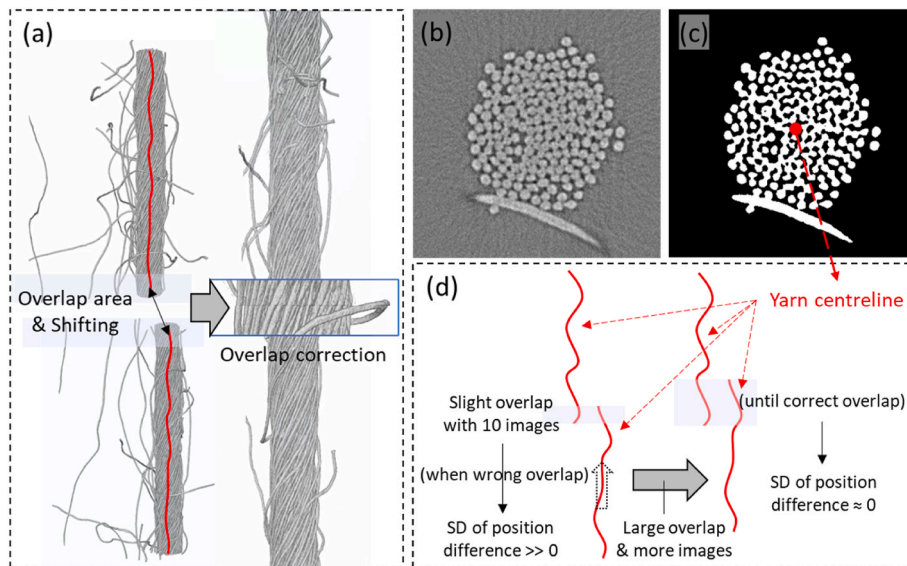

Fig. 2. The approach of image processing and µCT data stitching: (a) Overlap and shifting between two adjacent scanned segments (b) Original cross-sectional image (c) Fibre areas after Threshold and Median Filter (central point marked in red) (d) Determination of overlap area with minimum standard deviation (SD) of position differences.
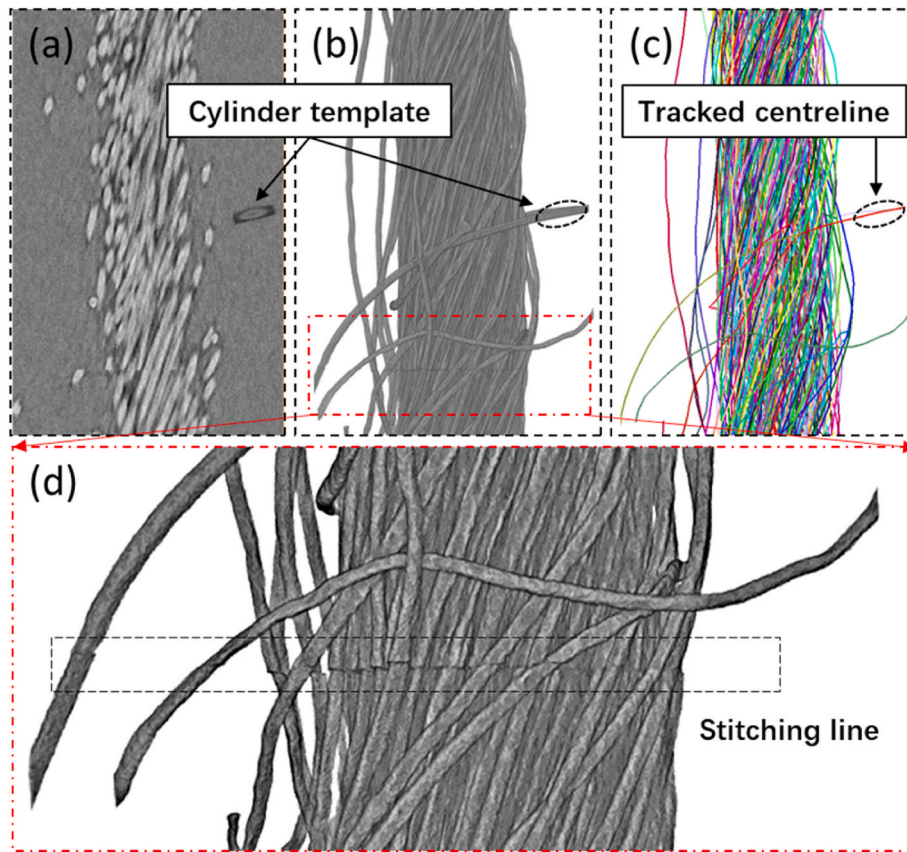
Fig. 3. Cylinder template in (a) 2D, (b) 3D view and (c) tracked centrelines for individual fibres (d) Details of stitching area.

curved angle are defined by the Cylinder Length and Angular Sampling parameters. The Outer Cylinder Radius and Mask Cylinder Radius set the upper and lower limits of the radius range (4–6 μm) for detecting cylinder structures, with an approximate 5 μm radius used of individual fibre in this study. And Inner Cylinder Radius is set to 0 reflecting the solid nature of the fibres.

ii) The Cylinder Correlation module correlates the fibre template with the μCT datasets in all orientations, assigning each fibre segment a score (Seed Correlation).

iii) The Trace Correlation Lines module maps the centrelines of cylinder-like structures. It begins at a fibre segment with a correlation value exceeding the Minimum Seed Correlation. Two key parameters, Minimum Continuation Quality and Direction Coefficient, determine the continuity and directionality when connecting fibre segments into a continuous fibre. To prevent excessive tracking, a minimum distance of 7 μm is set between two centrelines, and a minimum length of 250 μm is established to disregard ultra-short centrelines. The Avizo software automatically configures parameters for the Search Cone of centreline connection. Table 2 provides a detailed list of all parameters used in these modules.

iv) The Trace Correlation Lines module outputs Spatial Graph results, as depicted in Fig. 3c. Essential statistics, including chord length, curved length, and coordinates of each point in the centrelines, are extracted from the Spatial Graph. These data are then compiled in an Excel spreadsheet, with each set of statistics linked to its corresponding fibre number.

3. Development of image-based FE model and experimental setup

Moving beyond the traditional numerical models with uniform

Table 2
Parameters used in fibre centreline tracking.

Modules in Avizo	Parameters	Value
Cylinder correlation	Cylinder Length (μm)	20
	Angular Sampling	5
	Mask Cylinder Radius (μm)	5.5
	Outer Cylinder Radius (μm)	4
	Inner Cylinder Radius (μm)	0
Trace Correlation Lines	Minimum Seed Correlation	80
	Minimum Continuation Quality	40
	Direction Coefficient	0.5
	Minimum Distance (μm)	7
	Minimum Length (μm)	250
Search Cone	Length (um)	30
	Angle (degree)	20
	Minimum Step Size (%)	10

alignment and continuous fibres (as shown in Fig. 4a), this section introduces the stepwise development of high-fidelity FE model based on the μCT characterisation. This includes defining the material anisotropy, characterising the properties of individual fibre, specifying the contact behaviour, and establishing the boundary conditions. The stretching of the yarn is simulated using Abaqus/Explicit and validated with experiment tests according to ASTM D2256 standard test method for tensile properties of yarns by the single-strand method.

3.1. Centreline-based model

Model development commences with the fibre centrelines obtained through μCT scanning. Given the quasi-circular cross-section and uniform diameter of approximately 10 μm for PET fibres, as shown in Fig. 2b, the fibre entities were generated in SolidWorks by sweeping the cross-section along their traced centrelines. These entities were then
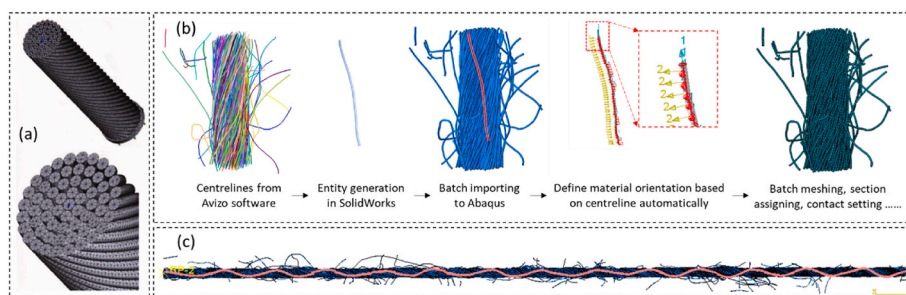
Fig. 4. (a) Traditional numerical models with uniform alignment [16], (b) Schematic diagram and workflow for the development of image-based model (one--segment data as example), (c) Numerical model of stitched-scanning data (with a highlighted through-length fibre).

imported into the finite element analysis software Abaqus, treating each fibre as an individual component. The purpose of creating discrete entities was to facilitate the meshing of three-dimensional solid elements in Abaqus, thereby enabling the analysis of interactions between fibres. During the batch import process of fibre entities, the material orientation of each fibre was determined using the Discrete Definition method, which relies on the normal axis for the outer surface and the primary axis for the fibre centrelines. Subsequently, the fibre entities underwent meshing using C3D8R elements with a global seed size of 15 μm, as illustrated in Fig. 4b. To ensure convergence in dynamic simulations, Distortion Control was employed with a length ratio of 0.1, and Hourglass Control was set to Enhanced.

3.2. Setting in FE model

In this study, PET fibres are characterised as anisotropic materials, with their material properties and contact behaviour outlined in Table 3. Due to the challenges in experimentally measuring properties transverse to the fibre direction for individual fibres, only the modulus in the fibre direction, denoted as E_1, was obtained through tensile tests on single polyester fibres (detailed in next section). Other material properties were sourced from previous literature and reasonable assumptions. The normal contact behaviour between fibres is defined as 'Hard' contact, with the tangential behaviour specified by a friction coefficient of 0.3. Contact initialisation is configured as 'Resolve with Strain-Free Adjustments' to prevent surface intersections of fibre entities in the initial state.

Boundary conditions (BCs) play a pivotal role in our simulations, dictating whether the helical structure of yarns twists or untwists under loading. The BCs are illustrated (in Fig. 6a) together with dynamic response in the discussion section. In this simulation, the cross-sections of fibres at the top and bottom sides are coupled to the central point of the section, with the bottom point fixed and a displacement applied to the top point along the yarn direction. Inspired by previous literature about yarn simulation [31,32], two distinct boundary conditions are investigated to simulate the stretching of a segment of the yarn without direct gripping: one with restricted rotation of the central points, simulating the stretching with clamped ends of the yarn model, and the other without restricting rotation, simulating the displacement-induced

tension of a segment in long yarn structures. Aligned with the loading speed of 100 mm/min in the experimental setup, the yarn model is stretched to 20 %–30 % strain in the finite element simulation, executed in Abaqus/Explicit for the dynamic process. To expedite computation, a mass-scaling factor of $1 \times E+9$ is applied, and the computation is performed in single precision on a workstation equipped with 40 processors.

3.3. Experimental tests

Tensile properties of individual PET fibres were determined using Dia-stron® LEX820 extensometer, as shown in Fig. 5a. The PET single fibres were mounted from both ends on specially designed plastic mounting tabs using UV setting glue (Dymax Ultralight weld). The detailed procedure of sample preparation is given elsewhere [37]. The prepared fibre samples were carefully transferred to the measuring unit of the instrument with the help of a special lifting device. The tensile tests were carried out with a 20 mm gauge length at an extension rate of 6 mm/min. The diameter of PET fibres (used in calculation of tensile stress) was determined with the help of scanning electron microscope (Jeol JSM-6610, Japan). The results, illustrated in Fig. 5b, reveal a stiffness of 7.02 ± 0.42 GPa, which would be used as the elastic modulus in fibre direction in subsequent FE modelling. It is important to mention that PET fibres exhibit viscoelastic behaviour, characterised by hysteresis in the stress-strain curve, as evident in Fig. 5b. Given the complexity of modelling the viscoelastic and plastic properties of anisotropic materials and the significant computational demands involved, this simulation simplifies the material properties by treating the PET fibres as purely elastic. Additionally, tensile tests yielded an average tensile strength of 658 ± 52 MPa, but the failure criteria for anisotropic fibres are not fully understood yet. Determining relevant failure parameters in different material orientations is still challenging. Therefore, the following numerical study focuses exclusively on the elastic behaviour and dynamic migration of fibres, using the tensile strength as a benchmark for comparison with the maximum principal stress, serving as a reference for potential failure.

Tensile tests of 100 % PET ring spun yarn were carried out following ASTM D2256 standard test method with a little modification on James Heal Titan Universal Strength Tester using 100 N load cell (as shown in Fig. 5c). This study aimed to experimentally investigate the effect of gauge length on the tensile behaviours of yarns. A sophisticated testing instrument, operating on the constant rate of extension (CRE) principle, was utilised, ensuring consistent performance regardless of the gauge length of the test specimen. The instrument's advanced load cell continuously recorded the applied force in real time as the specimen underwent deformation at a constant rate, enabling precise measurement of strain against applied force or stress. In accordance with the ASTM D2256 standard, the instrument automatically adjusted the extension rate to ensure the specimen's time to break was 20 ± 3 s. For 20's Ne staple-spun ring yarns, the typical extension rate for a 20 ± 3 s time to break was approximately 100 mm/min. Consequently, yarns

Table 3
The material properties and contact behaviours [32–36].

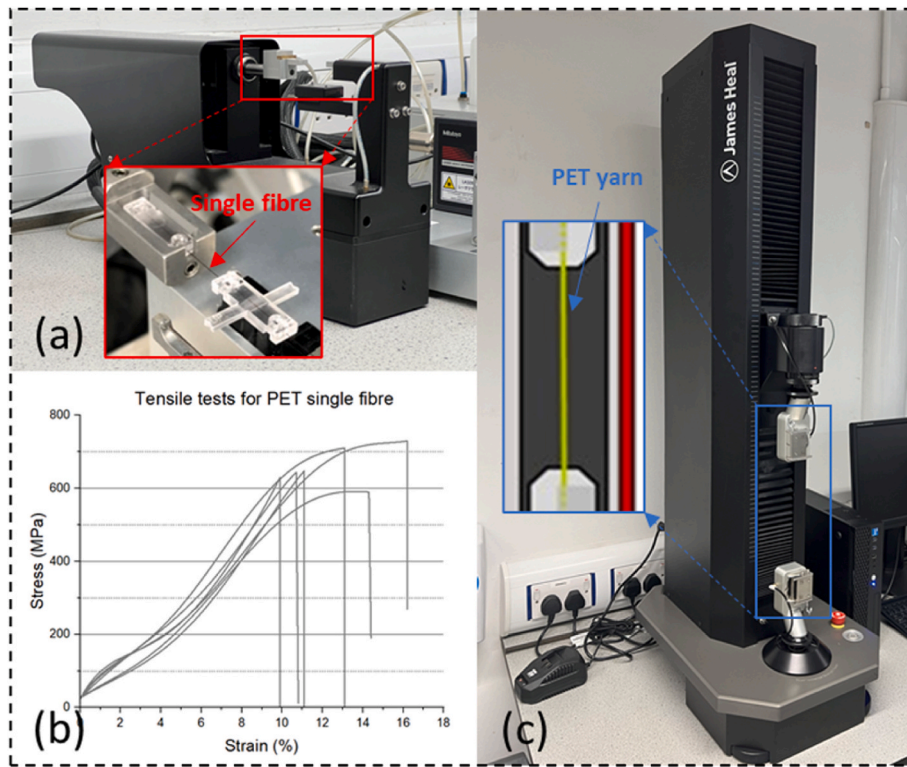|	Parameters	Value
Material properties	Density	1.38 g/cm³
	E_1	7.02 GPa
	E_2 & E_3	1.14 GPa
	v_{12} & v_{13}	0.34
	v_{23}	0.3
	G_{12} & G_{13}	0.85 GPa
	$G_{23} = E2/2(1+v23)$	0.41 GPa
Contact properties	Normal behaviour	Hard contact
	Tangential behaviour	Friction coefficient = 0.3

Fig. 5. (a) Tensile tests of single polyester fibre, (b) Experimental results of single-fibre tension and (c) Standard test method for tensile properties of yarns.

were tested at gauge lengths of 30, 50, 100, and 250 mm, all at a constant extension rate of 100 mm/min. Twenty specimens were tested for each gauge length to compute the average values.

4. Results and discussion

To visualise the dynamic response of yarn stretching and fibre migration, models from a single scanning segment are initially presented. Following this, the numerical results derived from the models based on the stitched scanning dataset are compared and validated against the experimental tests of ring-spun yarn. Crucially, the simulation offers valuable insights into the analysis and interaction between individual fibres, including stress, migration, and fibre-to-fibre friction. Finally, a parametric analysis is conducted using the developed image-based models to explore the influence of the friction coefficient between fibres on the yarn's mechanical response.

4.1. Dynamic response of yarn and fibre

Two distinct boundary conditions (BCs), one with restricted rotation at both ends and one without, were applied to a single-segment model measuring 0.8 mm in length. As illustrated in Fig. 6, only one segment was chosen to facilitate clearer visual comparisons due to its fewer, shorter fibres.

Without restricted rotation: The yarn exhibits untwisting behaviour. At 5 % strain, no significant increase in fibre stress is observed. By 10 % strain, the untwisting process is nearly complete, and an increase in stress is seen in fibres near the centre of the yarn structure. Subsequently, the fibres are gradually stretched and straightened, stabilising the overall yarn structure, while discontinuous 'hair fibres' progressively move away from the main yarn body.

With restricted rotation: The yarn shows enhanced twisting. An increase in fibre stress is noticeable at just 5 % strain, with a more uniform
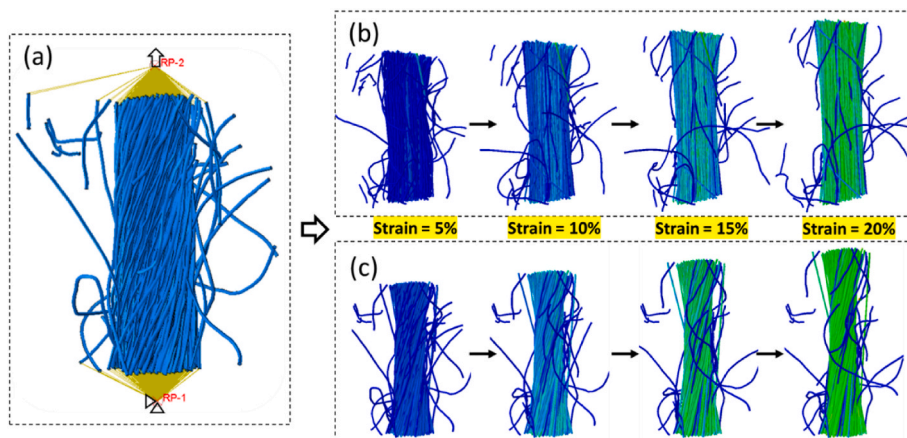

Fig. 6. (a) Boundary conditions of yarn structure in two ends (b) Yarn dynamic response of one-segment μCT data without and (c) with restricted rotation of end points.

stress increase observed between 10 % and 20 % strain. The yarn's midsection diameter is significantly reduced, with some discontinuous fibres being trapped within the core due to the enhanced twisting, while only a few 'hair fibres' move away from the body.

The FE models also offer valuable insights into individual fibres within yarn structures, and a level of detail unattainable through experimental tests. Fig. 8 illustrates the interaction between dynamic fibre migration and their stress evolution. Seven representative fibres (RFs) are randomly selected across a range of stress values, with their highlighted morphologies at 0 % (Fig. 7a) and 20 % (Fig. 7b–d) yarn strain. The mean values of maximum principal stresses for individual fibres are calculated to show the progressive evolution during tensile tests. Additionally, the percentage of fibres experiencing stress values exceeding 658 MPa is depicted, serving as a reference for potential fibre breakage.

In the BCs without end-point rotation restrictions, RF1 experiences abnormal tension due to the opposing untwisting of the yarn structure, leading to extremely high stress values. As the yarn reaches 20 % tensile strain (as shown in Fig. 7b), fibres RF2 to RF6 become increasingly stretched and straightened with those closer to the yarn's centre exhibiting higher stress values. The stress-strain curve for RF2 shows a steep and stable slope almost from the beginning, as RF2 is centrally located within the structure and undergoes minimal migration. Consequently, its stress value rises rapidly during stretching, eventually exceeding the tensile strength of a single fibre. Some outer fibres, such as RF5 and RF6, display a gradual increase in stress during the initial stage of yarn untwisting, followed by a more pronounced stress increase after 10 % tensile strain. This indicates that fibres near the centre, with lower initial migration, are more likely to break first, with failure gradually progressing to outer fibres as the yarn untwists and tightens. RF7, located at the outer edge, behaves like a hair fibre within the yarn structure. Without end-point restriction, one of its ends gradually moves away from the main body during untwisting, experiencing almost no stress increase throughout the stretching process.

For comparison, the mechanical responses of the same RF1-RF7 fibres are presented in Fig. 7d for the model with restricted rotation. A similar pattern emerges, with centrally located fibres like RF2 and RF3, which exhibit lower migration, showing rapid stress increase. Despite being at the outermost edge, RF1 exhibits a smaller stress value than RF6 due to its lower migration. Unlike the previous boundary condition, the fibres are under tension but not fully straightened, with the yarn's twisting structure significantly enhanced (as shown in Fig. 6c). After dynamic fibre migration, most fibres concentrate in the centre of the main body at 20 % tensile strain. Additionally, the hair-like RF7 fibre does not detach from the main body due to the enhanced twisting. Friction between fibres causes RF7 to record a higher stress value than in

the model without rotation restriction.

4.2. Yarn mechanical performance and individual fibre analysis

The tensile testing of the ring-spun yarn samples was examined using a range of gauge lengths, spanning 30, 50, 100 and 250 mm, and their results are shown in Fig. 8a. It can be observed that all the yarn samples failed at a similar maximum load, but the ones with shorter gauge lengths exhibited larger failure strains. This is because, for the tested yarn with shorter gauge length, the most of fibres were gripped at both ends by the two jaws. This reduced the fibre slippage when the overall yarn structure failed [38]. As a result, these gripped fibres were able to bear the load even after the yarn structure was destroyed, significantly increasing the failure strain of the tested sample [39].

The numerical simulations based on one-segment models exhibit stiffness values significantly higher than those obtained from experimental results. This discrepancy can be attributed to the fact that the 0.8 mm length is substantially shorter than the each turn of yarn twist in ring-spun yarn, rendering these μCT-based models are inadequate for accurately predicting the yarn's mechanical response. To improve the representativeness of the μCT dataset, especially for anisotropic fibrous materials, the implementation of a stitched scanning technique is recommended. In contrast, the numerical results derived from the stitched μCT dataset show trends consistent with experimental data, with a slope closely matching that of the force-strain curves for ring-spun yarn samples with 30 mm and 50 mm gauge lengths. This consistency indicates that μCT-based models from stitched scanning can reliably predict mechanical performance and offer robust basis for in-depth analysis of dynamic fibre migration.

The model without restricted end-point rotation (free end-point rotation), displays a small section with no recorded force due to slack in the yarn samples. As tension increases, the reaction force rises, and the unrestricted ends allows the twist in the ring-spun yarn to unwind, causing the outer fibres near the ends to detach the main yarn body and gradually straighten (Fig. 8b and c). This process is accompanied by an increase in the slope of the force-strain curve. At 15 % tensile strain, the untwisting of the ring-spun yarn is completed, and most fibres are fully stretched, resulting in a stable slope of the curve and stiffness of structure, with the yarn's main body maintaining a consistent diameter along its length.

The model with restricted end-point rotation (fix end-points), shows a stable slope of force-strain curve after the initial slack in the yarn is eliminated. As the samples are stretched, the twist in the yarn structure is further intensified, leading to a significant reduction in yarn diameter during the tensile test (as shown in Fig. 8d and e). Fig. 8 f further compares the yarn cross-section between different strain stages of this
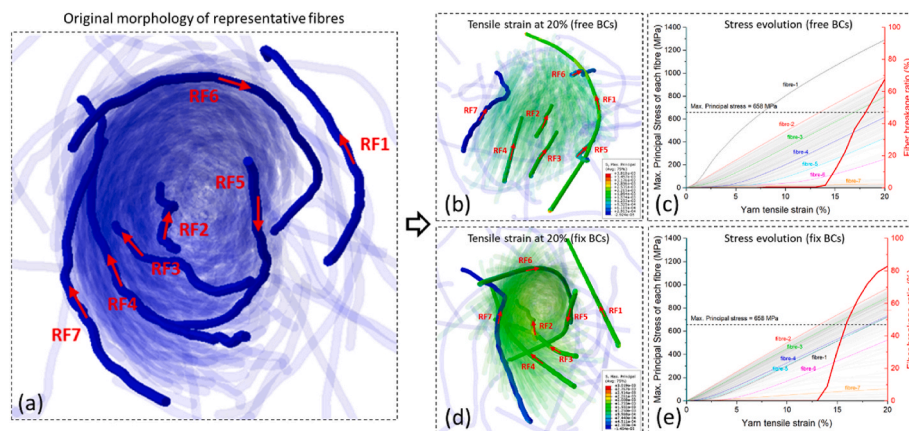

Fig. 7. One-segment model: (a) original morphology (b) & (c) fibre migration and stress evolution without restricted rotation (d) & (e) fibre migration and stress evolution with restricted rotation.
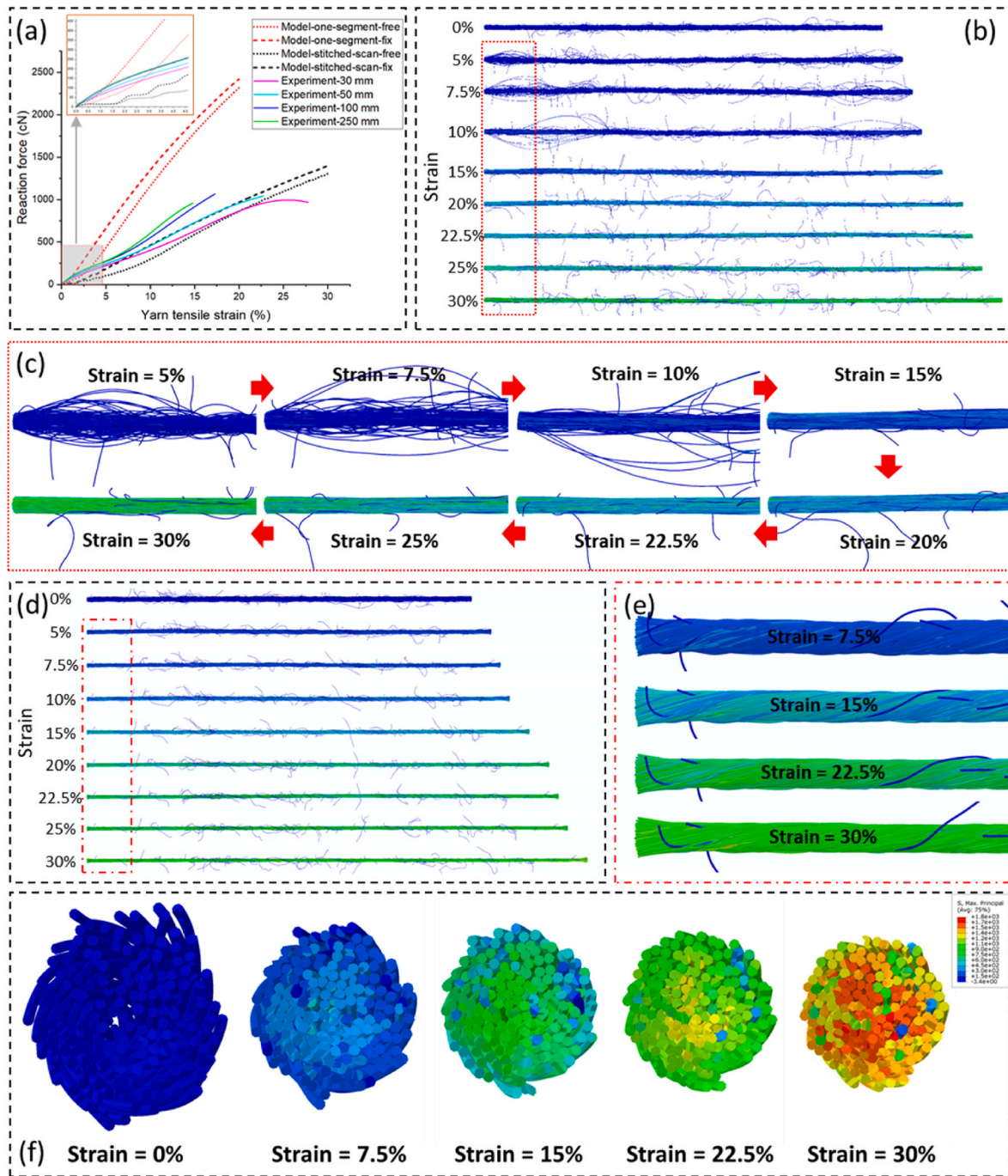
Fig. 8. (a) Force-strain curves with validation of experiment results and analysis of stitched-scanning model and detailed fibre migration (b) & (c) without and (d) & (e) with restricted rotation of end points (f) Comparison of yarn cross-section between different strain stages (with restricted rotation).

case, showing the contraction effect on yarn structure and the concentrated stress on the fibres located inside the yarn. This enhanced twisting also results in a higher recorded reaction force compared to the model with free ends. Additionally, the numerical results for the restricted rotation model demonstrate a dynamic fibre migration similar to that observed in the experimental test. This phenomenon is consistent with the previous research [40], which noted that there is enough friction between fibres to resist tensile load at higher twist level preventing fibre slippage until fibre breakage occurs (fibre breakage failure mechanism). Therefore, the following discussion will focus on the models with boundary conditions that restrict the rotation of end points, exploring their implications for yarn behaviour and performance.

Unlike traditional numerical simulations that rely on simplified

assumptions of uniform twisting geometry, μCT-based models offer a more refined approach by capturing the distinct behaviour of each fibre as it migrates within the yarn. The analysis of stitched scanning datasets, enables the investigation of stress evolution, frictional force development, and dynamic migration progression, shedding light on their intricate relationships. The subsequent discussion focuses on the model with restricted rotation, owing to its better representativeness and similarity to experimental tests.

The morphologies of six representative fibres at 0 % and 30 % yarn strain highlighted in black and other colours respectively are presented in Fig. 9b. The most stress-strain curves of individual fibres show a small initial slope (as shown in Fig. 9a), as no fibre consistently maintains position at the centre with a low original migration throughout the

lengthy yarn. For instance, although RF1 is partially centred, it migrates to the outer edge during dynamic loading with the yarn's partial spinning. Notably, the long but discontinuous RF1 experiences greater stress than continuous fibres RF2 and RF3 because of its lower original migration, whereas there is a greater migration factor for RF2 and RF3 fibres and they wind along the yarn length with constant cycle. The enhanced twisting prevents RF1's free end from leaving the main yarn body, highlighting that a fibre's original migration and position significantly impact its stress and breakage probability more than its length and continuity. A comparison of short, discontinuous fibres RF4 and RF5 reveals that RF4's free end remains within the main body during stretching, resulting in higher stress whereas RF5's free end moves away, influencing its stress distribution. Fig. 9 explains this phenomenon which indicates that the position of the free end and its dynamic migration significantly influence a fibre's stress distribution. Considering that continuous fibres are rare in longer yarn structures (over 100 mm in length), RF1, RF4, and RF5 are more representative, underscoring the importance of migration analysis. The extremely short and discontinuous RF6 experiences negligible stress throughout the process, gradually moving away from the main body. Such hair-like fibres when released or fractured may lead to microplastic pollution in the subsequent manufacturing, use, and service life of textiles.

The finite element model exports the frictional force at each node, allowing the calculation of the mean frictional force for each fibre. This calculation considers only the nodes with fibre-to-fibre interaction, defined as nodes where the normal contact force is greater than zero. Specifically, the mean value of the frictional force is determined by dividing the total frictional force on the fibre or yarn with the number of contact nodes. This approach ensures a more accurate comparison of the frictional behaviour among fibres of varying lengths. Additionally, it eliminates the influence of hair fibres, further refining the analysis. The red dotted line represents the mean frictional force across all nodes, serving as a measure of the overall structure's frictional behaviour. Initially, the frictional force increases rapidly as the yarn's slack is replaced by stretching as shown in Fig. 10a, and fibres in the twisted structure come into full contact and move relative to each other. As the curve's slope decreases, fibres press against and lock each other during enhanced twisting, reducing relative movement as most fibres tend to stretch collectively in the later stages. Notably, among individual fibres, RF1 shows the highest mean friction force due to its central position and the strong compression within the yarn structure. RF2 and RF3 exhibit similar values, despite significant differences in their principal stress as their relative position along the yarn length renders their frictional behaviour, more dependent on location and interactions with neighbouring fibres. In contrast, discontinuous fibres RF4 and RF5 display similar values until 5 % yarn strain, after which differences emerge as RF5's free end moves away from the main body, reducing fibre-to-fibre interaction and frictional behaviour. Fig. 10b illustrates the normal contact behaviour of individual fibres and the yarn. The observed trends in the normal contact forces of representative fibres closely resemble their frictional behaviour, confirming that mutual squeezing between fibres during yarn stretching is a critical factor in enhancing friction. The

notable difference lies in the fact that the normal contact forces of certain fibres do not begin at zero. This is attributed to the model's mesh adjustment mechanism for handling fibre overclosure, which leads to the presence of initial contact pressure.

The fibre migration represents the relative movement of a fibre with respect to its neighbouring fibres and its ultimate radial position along the yarn length [41]. Traditionally, fibre migration analysis has been limited to studying the geometrical arrangement of fibres in the initial state of yarn structure as captured from the produced textile. However, the more interesting and dynamic evolution of fibres' position and movement overtime remains unclear primarily due to the challenges in micro-characterising the fibres under loading conditions. Driven by the image-based model in this study, the dynamic migration analysis of each individual fibre can be performed, providing a new perspective for studying the mechanical response mechanisms of the yarn structure.

In this study, the dynamic fibre migration is calculated by adopting the parameters suggested by John Hearle in a study [42]. The description of location variations of fibre segments begins from the fibre position $Y = (r/R)^2$ along the yarn length, where R is the yarn radius and $r = \sqrt{(x_i - x_c)^2 + (y_i - y_c)^2}$ is the distance between the observed fibre segment/point and the yarn's centreline. The fibre centrelines' segments and their corresponding coordinates (x_i, y_i, z_i) of points are obtained from centreline tracking process detailed above, while the central point (x_c, y_c) and the yarn radius are obtained from above analysis along the yarn cross section. The migration parameters, including mean fibre position ($\overline{Y}$), root mean square (RMS) deviation (mean amplitude of migration, $\overline{D}$), mean migration intensity (I) as introduced by Ref. [42] and migration factor (K) as proposed by Ref. [43] to represent the total migration in yarn and plotted in Fig. 10c, can be expressed as:

$$\text{Mean fibre position} : \overline{Y} = \sum_{i=1}^{n} \frac{(r/R)^2}{n}$$

Mean Amplitude of Migration (RMS deviation)

$$: \overline{D} = \left\{ \sum_{i=1}^{n-1} \frac{(Y_i - \overline{Y})^2}{n} \right\}^{1/2}$$

$$\text{Mean migration intensity} : I = \left[\sum_{i=1}^{n-1} \left\{ \frac{(Y_{i+1} - Y_i)}{(z_{i+1} - z_i)} \right\}^2 \middle/ n \right]^{1/2}$$

$$\text{Migration factor} : K = \overline{D} * I$$

where there are n observations of fibre position Y along the yarn longitudinal axis z_i.

The majority of long fibres tend to migrate towards the yarn's centre axis and elongate under tensile loading, leading to a decrease in migration factor (as seen with RF1 to RF3). A comparative analysis of these fibres reveals that their original migration factor is crucial to a fibre's mechanical response; fibres with lower migration factors experience a significant stress increase and are more prone to breakage.
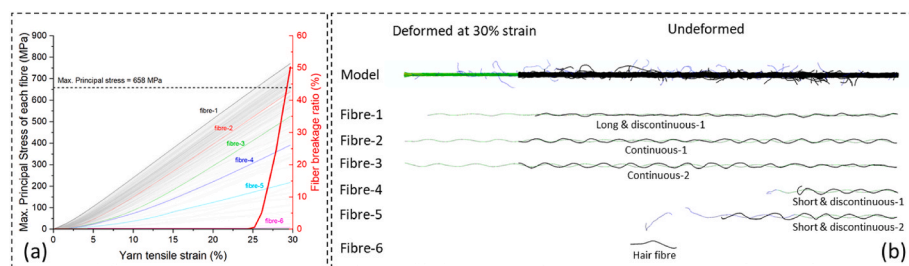

Fig. 9. Stitched-scanning model with restricted rotation: (a) Distribution for the mean value of Max. principal stress for each individual fibre (b) Analysis of representative fibres when strain = 0 % and 30 %.
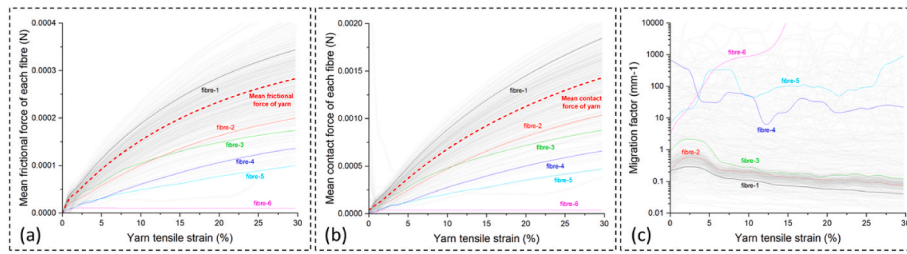
Fig. 10. Evolution of (a) mean value of frictional force, (b) mean value of normal contact force and (c) migration factor for each individual fibre from stitched-scanning model with restricted rotation.

RF4's original migration factor is higher than RF5's, but RF4's value decreases during stretching while RF5's value increases due to its free end moving away from the main body. In contrast, RF6's migration factor increases rapidly, reflecting the behaviour of short, discontinuous fibres. These changes in migration factor align with the fibre displacement patterns shown in Fig. 9b, confirming the reliability of fibre migration statistics and providing insights into stress and frictional force evolutions in individual fibres. In general, fibre position and migration are critical determinants of mechanical response. During dynamic stretching, most discontinuous fibres' free ends remain within the main body due to enhanced twisting and fibre-to-fibre friction, ensuring continuous load transfer and highlighting the complex interactions governing fibre behaviour.

4.3. Parametric analysis of friction coefficient

The frictional interaction between fibres is a key aspect of yarn structure influencing its mechanical performance. To study this effect, three friction coefficients with values 0.1, 0.3, and 0.5 (designated as f1, f3, and f5, respectively) were selected to compare the differences in mechanical performance, including reaction force, mean principal stress, and mean frictional force (see Fig. 11). This parametric analysis focuses on the restricted rotation model, as frictional behaviour has a more pronounced impact on the enhanced twisting structure. A friction coefficient of 0.1 shows a significant reduction in fibre-to-fibre friction, leading to decreased yarn reaction force and individual fibre stress. The weak friction involves sliding of the fibres in the yarn over each other under stretching load (so called fibre slippage failure mechanism) [40], highlighting the importance of fibre-to-fibre friction in yarn structure. Conversely, a friction coefficient of 0.5 presents similar mechanical responses to 0.3. The increase in fibre friction from 0.3 to 0.5 does not influence the reaction force and stress remain much, suggesting that a friction coefficient of 0.3 is sufficient to support the "mutual locking" of the yarn structure under enhanced twisting. Here, the mechanical response depends primarily on the structure itself and the fibres' stiffness and strength. However, in reality, fibre frictional behaviour is more complex with factors like fibre cross-sections deformation under pressure during enhanced twisting, leading to inconsistent frictional properties along their length. This study only alters the overall friction

coefficient for a specific yarn structure, implying that the friction coefficient required for 'mutual interlocking' may vary depending on different textile manufacturing methods and yarn structures. In another study, it has been demonstrated that altering friction characteristics of textile materials leads to change in the release of fragmented fibres (microplastics) from textiles [44].

5. Conclusion

This research presents a µCT image-based model for investigating the mechanical behaviour of ring-spun yarn utilising datasets of two different lengths. The longer 15 mm model demonstrated superior accuracy when compared to experimental data. By applying boundary conditions that restricted rotation at both ends, the model effectively captured the mechanical response and structural evolution, aligning with the dynamic processes observed in yarn tensile tests.

Microscopic analysis of individual fibres within the µCT image-based model revealed that a fibre's initial position and migration factor significantly influence its stress evolution. Fibres situated closer to the yarn's centre experience a rapid increase in stress during stretching, potentially initiating fibre breakage at the centre and progressing outward. The location of fibre free ends and their subsequent migration also significantly affect the mechanical response. In a structure with enhanced twisting, the free ends near the centre keep locked within the main body due to inter-fibre friction, facilitating continuous load transfer. In contrast, fibres near the outer edge tend to detach from the yarn, exhibiting lower stress and consequently reducing the overall stiffness of the structure. A parametric study of frictional behaviour indicated that a friction coefficient of 0.1 was insufficient to support fibres' mutual locking for this specific yarn structure, leading to noticeable changes in mechanical response. However, friction coefficients of 0.3 and 0.5 had minimal impact on the results, suggesting that once the structure is tightly twisted, the mechanical response is primarily governed by fibre stiffness and strength.

The finite element modelling approach introduced in this paper facilitates micro-analysis of fibre interactions in anisotropic materials, utilising in-situ fibre orientation, length, and continuity data obtained from µCT scanning. These findings enhance our understanding of how material irregularities impact mechanical performance. The modelling
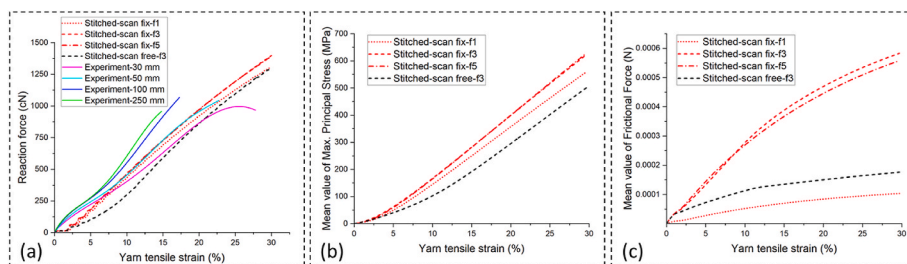

Fig. 11. Parametric study of friction coefficient: (a) Mechanical response of yarn tensile test (b) Mean value of Max. principal stress of fibres, and (c) Mean value of frictional force of fibres.

method can be applied to the analysis of underlying formation of microplastics from textiles and textile materials in general as well as fibre-reinforced composites textile structures and fibre-reinforced composites, offering valuable insights into material constitutive behaviour and failure mechanisms. Several scientific challenges remain to be addressed, including the characterisation of viscoelastic, plastic and failure properties of anisotropic fibres and definition of complex frictional behaviour through micro/nano testing. Furthermore, when dealing with non-circular fibres and blended fibres in the textile manufacturing, new entity generation methods and models need to be developed based on the improved image processing techniques for μCT data.

CRediT authorship contribution statement

Haoqi Zhang: Writing – original draft, Software, Methodology, Investigation, Formal analysis, Data curation, Conceptualization. **Abdul Jabbar:** Writing – original draft, Methodology, Investigation. **Aonan Li:** Software, Data curation. **Xinxin Wang:** Software, Data curation. **Dongmin Yang:** Writing – review & editing, Software, Resources, Methodology, Funding acquisition, Conceptualization. **Muhammad Tausif:** Writing – review & editing, Resources, Methodology, Funding acquisition, Conceptualization.

Declaration of competing interest

The authors declare that they have no known competing financial interests or personal relationships that could have appeared to influence the work reported in this paper.

Acknowledgement

Appendix A. Supplementary data

Supplementary data to this article can be found online at https://doi.org/10.1016/j.compscitech.2025.111036.

Data availability

Data will be made available on request.

References

[1] K. Fujihara, et al., Fibrous composite materials in dentistry and orthopaedics: review and applications, Compos. Sci. Technol. 64 (6) (2004) 775–788.

[2] J. Zhang, G. Lin, U. Vaidya, H. Wang, Past, present and future prospective of global carbon fibre composite developments and applications, Compos. B Eng. 250 (2023) 110463.

[3] J. Zhang, V.S. Chevali, H. Wang, C.-H. Wang, Current status of carbon fibre and carbon fibre composites recycling, Compos. B Eng. 193 (2020) 108053.

[4] J. Liu, et al., Microfiber pollution: an ongoing major environmental issue related to the sustainable development of textile and clothing industry, Environ. Dev. Sustain. 23 (8) (2021) 11240–11256.

[5] H. Zhang, D. Yang, Y. Sheng, Performance-driven 3D printing of continuous curved carbon fibre reinforced polymer composites: a preliminary numerical study, Compos. B Eng. 151 (2018) 256–264.

[6] J. Karger-Kocsis, H. Mahmood, A. Pegoretti, All-carbon multi-scale and hierarchical fibers and related structural composites: a review, Compos. Sci. Technol. 186 (2020) 107932.

[7] X. Li, L.G. Tabil, I.N. Oguocha, S. Panigrahi, Thermal diffusivity, thermal conductivity, and specific heat of flax fiber–HDPE biocomposites at processing temperatures, Compos. Sci. Technol. 68 (7–8) (2008) 1753–1758.

[8] X. Zhang, S. Fujiwara, M. Fujii, Measurements of thermal conductivity and electrical conductivity of a single carbon fiber, Int. J. Thermophys. 21 (2000) 965–980.

[9] C. Unterweger, et al., Impact of fiber length and fiber content on the mechanical properties and electrical conductivity of short carbon fiber reinforced polypropylene composites, Compos. Sci. Technol. 188 (2020) 107998.

[10] I. Floris, J.M. Adam, P.A. Calderón, S. Sales, Fiber optic shape sensors: a comprehensive review, Opt Laser. Eng. 139 (2021) 106508.

[11] S. Bahl, A.K. Bagha, Finite element modeling and simulation of the fiber–matrix interface in fiber reinforced metal matrix composites, Mater. Today: Proc. 39 (2021) 70–76.

[12] H. Xu, J. Zhou, X. Cao, D. Yu, C. Miao, Simulations of the interaction between fiber bundles/yarns and the energy absorption of the fabric under hypervelocity impact, Int. J. Impact Eng. 181 (2023) 104733.

[13] L. Daelemans, et al., Finite element simulation of the woven geometry and mechanical behaviour of a 3D woven dry fabric under tensile and shear loading using the digital element method, Compos. Sci. Technol. 137 (2016) 177–187.

[14] L. Daelemans, et al., Kinematic and mechanical response of dry woven fabrics in through-thickness compression: virtual fiber modeling with mesh overlay technique and experimental validation, Compos. Sci. Technol. 207 (2021) 108706.

[15] K. Sriprateep, CAD/CAE for stress–strain properties of a wide range of multifilament twisted man-made filament yarns, Textil. Res. J. 89 (2) (2019) 204–215.

[16] K. Sriprateep, E.L. Bohez, CAD/CAE for stress–strain properties of multifilament twisted yarns, Textil. Res. J. 87 (6) (2017) 657–668.

[17] S. Vassiliadis, A. Kallivretaki, C. Provatidis, Mechanical modelling of multifilament twisted yarns, Fibers Polym. 11 (2010) 89–96.

[18] L. Wan, Y. Ismail, Y. Sheng, J. Ye, D. Yang, A review on micromechanical modelling of progressive failure in unidirectional fibre-reinforced composites, Composites Part C: Open Access 10 (2023) 100348.

[19] N. Balasubramani, B. Zhang, N. Chowdhury, A. Mukkavilli, M. Suter, G. Pearce, Micro-mechanical analysis on random RVE size and shape in multiscale finite element modelling of unidirectional FRP composites, Compos. Struct. 282 (2022) 115081.

[20] M. Alves, C.C. Junior, S.K. Ha, Fiber waviness and its effect on the mechanical performance of fiber reinforced polymer composites: an enhanced review, Compos. Appl. Sci. Manuf. 149 (2021) 106526.

[21] K. Sreprateep, E.L. Bohez, Computer aided modeling of fiber assemblies, Comput. Aided Design Appl. 3 (1–4) (2006) 367–376.

[22] K. Sriprateep, E. Bohez, A new computer geometric modelling approach of yarn structures for the conventional ring spinning process, J. Textil. Inst. 100 (3) (2009) 223–236.

[23] K. Schröder, A. Zinke, R. Klein, Image-based reverse engineering and visual prototyping of woven cloth, IEEE Trans. Visual. Comput. Graph. 21 (2) (2014) 188–200.

[24] D.B. Aychilie, Y. Kyosev, M.A. Abtew, Automatic modeller of textile yarns at fibre level, Materials 15 (24) (2022) 8887.

[25] A. Bral, L. Daelemans, J. Degroote, A novel technique to simulate and characterize yarn mechanical behavior based on a geometrical fiber model extracted from microcomputed tomography imaging, Textil. Res. J. 93 (9–10) (2023) 2042–2062.

[26] H. Zhang, J. Chen, D. Yang, Fibre misalignment and breakage in 3D printing of continuous carbon fibre reinforced thermoplastic composites, Addit. Manuf. 38 (2021) 101775.

[27] D. Yang, H. Zhang, J. Wu, E.D. McCarthy, Fibre flow and void formation in 3D printing of short-fibre reinforced thermoplastic composites: an experimental benchmark exercise, Addit. Manuf. 37 (2021) 101775.

[28] G. Gaiselmann, I. Manke, W. Lehnert, V. Schmidt, Extraction of curved fibers from 3D data, in: Forum Bildverarbeitung, KIT Scientific Publishing, 2012, p. 119.

[29] X. Huang, D. Wen, Y. Zhao, Q. Wang, W. Zhou, D. Deng, Skeleton-based tracing of curved fibers from 3D X-ray microtomographic imaging, Results Phys. 6 (2016) 170–177.

[30] P. Henyš, L. Čapek, Individual yarn fibre extraction from micro-CT: multilevel machine learning approach, J. Text. Inst. 112 (12) (2021) 1979–1985.

[31] Y. Wang, Y. Jiao, N. Wu, J. Xie, L. Chen, P. Wang, An efficient virtual modeling regard to the axial tensile and transverse compressive behaviors of the twisted yarns, J. Ind. Textil. 52 (2022) 15280837221137353.

[32] J. Wang, et al., Simulation and analysis of the twist propagation process of polyester staple yarn on the fiber scale, Textil. Res. J. 91 (7–8) (2021) 874–884.

[33] A.R. Bunsell, Handbook of Tensile Properties of Textile and Technical Fibres, Elsevier, 2009.

[34] C. Czibula, T. Seidlhofer, C. Ganser, U. Hirn, C. Teichert, Longitudinal and transverse low frequency viscoelastic characterization of wood pulp fibers at different relative humidity, Materialia 16 (2021) 101094.

[35] Q. Xiao, R. Wang, X. Lu, S. Zhang, S. Hongyu, Finite element modeling effects of fiber performance on pilling of polyester–cotton woven fabrics, Textil. Res. J. 92 (13–14) (2022) 2247–2264.

[36] S. Wu, J. Li, C. Yu, Simulation of fiber arrangement in slub strands and twisting on the slub yarn with the finite element method, Textil. Res. J. 93 (5–6) (2023) 1445–1455.

[37] H.D. Cochran, Analysis of Carbon Fiber Characterization Techniques, 2008.

[38] M. Realff, M. Seo, M. Boyce, P. Schwartz, S. Backer, Mechanical properties of fabrics woven from yarns produced by different spinning technologies: yarn failure as a function of gauge length, Textil. Res. J. 61 (9) (1991) 517–530.

[39] A. Ghosh, S. Ishtiaque, R. Rengasamy, Analysis of spun yarn failure. Part I: tensile failure of yarns as a function of structure and testing parameters, Textil. Res. J. 75 (10) (2005) 731–740.

[40] X. Yu, et al., Twisting in improving processing of waste-derived yarn into high-performance reinforced composite, J. Clean. Prod. 317 (2021) 128446.

[41] G. Tyagi, Yarn structure and properties from different spinning techniques, in: Advances in Yarn Spinning Technology, Elsevier, 2010, pp. 119–154.

[42] J. Hearle, B. Gupta, V. Merchant, Migration of fibers in yarns: Part I: characterization and idealization of migration behavior, Textil. Res. J. 35 (4) (1965) 329–334.

[43] Y. Huh, Y.R. Kim, W.Y. Ryu, Three-dimensional analysis of migration and staple yarn structure, Textil. Res. J. 71 (1) (2001) 81–89.

[44] M.B. Abdul Jabbar, Josh Armitage, Muhammad Tausif, Oxygen plasma treatment to mitigate the shedding of fragmented fibres (microplastics) from polyester textiles, Cleaner Energy Technol. Under review (2024).